ASSOCIATED CONTENT

Supporting Information.

Phase Controlled Growth of Cd_3As_2 Nanowires and Their Negative Photoconductivity

Kidong Park,[†] Minkyung Jung,[‡] Doyeon Kim,[†] Janice Ruth Bayogan,[§] Jong Hyun Lee,[†] Sung Jin An,[§] Jungpil Seo,[§] Jaemin Seo,[†] Jae-Pyoung Ahn,[¥] and Jeunghee Park*[,†]

[†] Department of Advanced Materials Chemistry, Korea University, Sejong 339-700, Republic of Korea

[‡] DGIST Research Institute, DGIST, Daegu 42988, Republic of Korea

[§] Department of Emerging Materials Science, DGIST, Daegu 42988, Republic of Korea

[¥] Advanced Analysis Center, Korea Institute of Science and Technology, Seoul 136-791, Republic of Korea

*E-mail: parkjh@korea.ac.kr (J.P.)

Content

Experimental Details

(1) Synthesis

Cd_3As_2 (99%, Alfa Aesar) powders were placed in ceramic boats, which are loaded inside a quartz tube reactor. A silicon (Si) substrate, on which a 5 nm-thick Au film was deposited, was positioned at a distance of 18 cm away from the powder source. Argon gas is continuously supplied at a rate of 500 sccm under ambient pressure during growth. The temperature of the powder sources is set to 450-650 °C. The substrate is maintained at T = 320-450 °C to synthesize the nanowires. The temperature of the source and substrate as well as the reaction time for each sample was summarized as follows.

Samples	Temperature of source (℃)	Temperature of substrates (℃)	Reaction time (min)
bct-Cd_3As_2	450	320	60
pt1-Cd_3As_2	500	350	40
pt12-Cd_3As_2	550	380	30
Pt21-Cd_3As_2	570	420	20
pt2-Cd_3As_2	650	450	10
Bi-Cd_3As_2	450	300	30

We also used a silicon substrate coated with 1 mM BiI_3 (99.999%, Sigma-Aldrich Corp.) in ethanol solution to form the Bi catalytic nanoparticles is positioned 8 cm away from the powder source. Argon gas is continuously supplied at a rate of 500 sccm under ambient pressure during growth. The temperature of the powder sources is set to 450 °C. The substrate is maintained at T ≈ 280-300 °C to synthesize the nanowires. The reaction time was 30 min.

(2) Characterization

The structure and composition of the products were analyzed by scanning electron microscopy (SEM, Hitachi S-4700), field-emission transmission electron microscopy (TEM, FEI TECNAI G^2 200 kV), high-voltage TEM (HVEM, Jeol JEM ARM 1300S, 1.25 MV), and energy-dispersive X-ray fluorescence spectroscopy (EDX). Fast Fourier-transform (FFT) images were generated by the inversion of the TEM images using Digital Micrograph GMS1.4 software (Gatan Inc.). A tilt holder (Dual Orientation Tomography Holder 927, Gatan Co.) was used for the TEM measurements. High-resolution XRD patterns were obtained using the 9B and 3D beam lines of the Pohang Light Source (PLS) with monochromatic radiation. XRD pattern measurements were also carried out in a Rigaku D/MAX-2500 V/PC using Cu K_α radiation (λ = 1.54056 Å). X-ray photoelectron spectroscopy (XPS) data were collected using the 10A2 beam line of the PLS with photon energy of 380 and 630 eV. XPS measurements were also performed using a laboratory-based spectrometer (Thermo Scientific Theta Probe) using a photon energy of 1486.6 eV (Al Kα).

(3) Fabrication of FET devices

For FET devices, Cd_3As_2 NW devices were fabricated on a highly doped p^{++} silicon substrate, which serves as a back gate, covered by 300 nm-thick thermally grown SiO_2. The trenches for the bottom gates are fabricated by electron beam lithography and anisotropic reactive ion etching with CF_4, followed by a wet etching step using buffered HF. The depth and width of these trenches are 100 nm and 300 nm, respectively. Ti/Au (5/25 nm) is deposited in the trenches to form the bottom gates. Subsequently, Cd_3As_2 NWs are transferred across the bottom gates. Finally, the separation (L) of Ti/Au (5/120 nm) contacts is defined after etching with Ar plasma to remove the native oxide at the surface of the NW. The NW is separated from the bottom gates by 70 nm, enabling

effective gating compared to the global back gate. Independent control of the bottom gates (V_L and V_R) enables us to change the local electronic potential of NW segments above theses gates. The NW lead and NW segments underneath the source-drain contacts are less affected by the bottom gating because of their distance from the gates. Therefore, these regions effectively remain in the intrinsic doping state, which is weak n–type. The devices are measured using a standard lock-in technique with a modulation frequency of 77 Hz and an excitation voltage of 200 μV.

(4) Calculation of carrier mobility

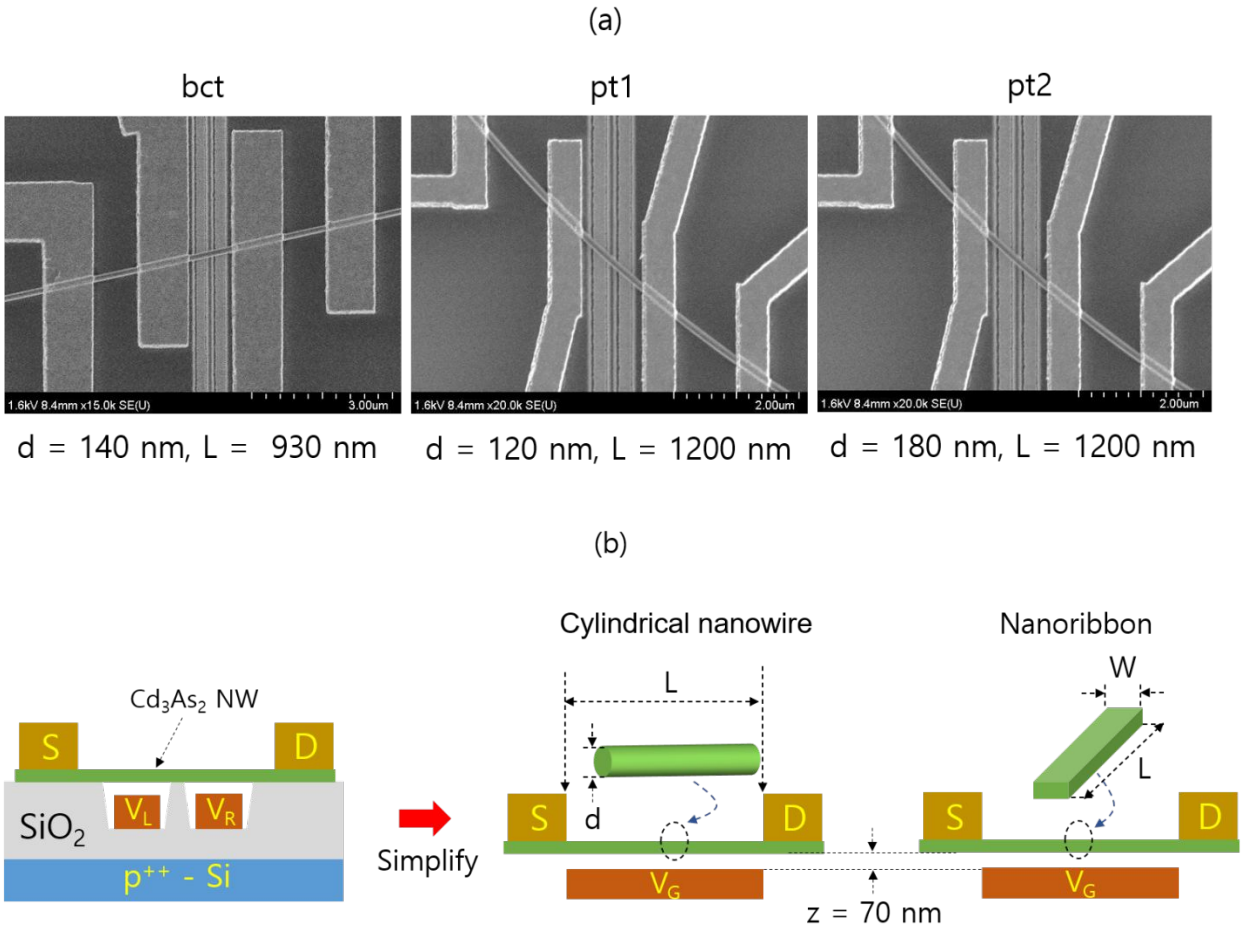

Figure E. (a) SEM images of four-terminal *bct*-, *pt-1*, and *pt2*-Cd_3As_2 NW FET device, showing the dimension of electrodes. (b) Schematic diagram for the NW FET devices and their simplified models assuming that the Cd_3As_2 NW would be the cylindrical nanowire and nanoribbon.

The dimension of *bct*-, *pt-1*, and *pt2*-Cd_3As_2 NW FET device are shown in Figure Ea. The general form of capacitance (C) for the cylindrical shaped nanowires is approximately

$$C \approx \frac{2\pi\varepsilon_0\varepsilon_r L}{\ln\left[\frac{4z+d}{d}\right]} \qquad (1),^{\text{S1-S3}}$$

where L is the channel length, z is the gate insulator thickness (= 70 nm), d is the nanowire diameter, and dielectric constant $\varepsilon_r = 1$ for vacuum.

If we use the parallel-plate capacitor model for the nanoribbon with an area of A (= width (W) × length (L)), the capacitance can be calculated by equation (3).

$$C = \frac{\varepsilon_0\varepsilon_r A}{z} \qquad (2)$$

Then the mobility (μ) was calculated using the following equation (3),

$$\mu = \frac{dG\ L^2}{dV_G\ C} \qquad (3),$$

where dG/dV_G is the transconductance, C is the capacitance, and L is the channel length. The transconductance was obtained from the slope of linear region of the conductance curve (G vs. V_G). The slope value was multiplied by e^2/h (=3.87×10^{-5} C^2 $J^{-1}s^{-1}$), yielding the dG/dV_G

The G measurement (at 10 K) for the FET device fabricated using the Cd_3As_2 NWs yielded the mobility as shown in the following table. By assuming that the capacitance of Cd_3As_2 follows the cylindrical wire model (see the scheme in Figure Eb) using the equation (1), the values are summarized below.

Cd_3As_2 NW	d (nm)	L (nm)	C (F)	slope	dG/dV_G	μ (cm^2 $V^{-1}s^{-1}$)
bct	140	930	4.67×10^{-17}	1.138	4.40×10^{-5}	8.2×10^{3}
pt1	120	1300	5.98×10^{-17}	0.320	1.23×10^{-5}	3.5×10^{3}
Pt2	180	1200	7.06×10^{-17}	1.065	4.12×10^{-5}	8.4×10^{3}

Mobility was calculated by assuming that the capacitance of Cd_3As_2 follows the parallel-plate

model (see the scheme in Figure Eb) using the equation (2). The width (W) is approximated by the diameter. The values are summarized below.

Cd_3As_2 NW	W (nm)	L (nm)	A (nm^2)	C (F)	dG/dV_G	μ ($cm^2\ V^{-1}s^{-1}$)
bct	140	930	1.30×10^5	1.65×10^{-17}	4.40×10^{-5}	2.3×10^4
pt1	120	1300	1.56×10^5	1.97×10^{-17}	1.23×10^{-5}	1.1×10^4
Pt2	180	1200	2.16×10^5	2.73×10^{-17}	4.12×10^{-5}	2.2×10^4

Using the parallel-plate capacitor model, the dG/dV_G as a function of temperature yielded the mobility as shown below.

W (nm)	L (nm)	C (F)	T (K)	slope	dG/dV_G	μ ($cm^2\ V^{-1}s^{-1}$)
180	1200	2.73×10^{-17}	4	1.068	4.13×10^{-5}	2.2×10^4
			8	1.064	4.12×10^{-5}	2.2×10^4
			10	1.065	4.12×10^{-5}	2.2×10^4
			15	1.038	4.05×10^{-5}	2.1×10^4
			20	1.029	4.01×10^{-5}	2.1×10^4
			40	0.970	3.75×10^{-5}	2.0×10^4
			60	0.887	3.43×10^{-5}	2.0×10^4
			80	0.795	3.07×10^{-5}	1.8×10^4
			100	0.697	2.70×10^{-5}	1.6×10^4
			200	0.353	1.37×10^{-5}	7.8×10^3
			300	0.0683	0.26×10^{-5}	1.5×10^3

(5) Fabrication of photodetector devices

Photodetector devices were fabricated as follows. Photolithography was used to deposit Ti (20 nm)/Au (80 nm) electrodes on a highly doped p^{++} silicon (B-doped with a resistivity of < 0.005

Ω·cm) substrate, with a 300-nm-thick thermally grown silicon oxide layer, by sputtering using a patterned mask. The NWs were dispersed by applying a drop of its IPA solution onto a patterned Si substrate. The samples were then coated with a layer of poly(methyl methacrylate) (PMMA, A4, Microchem. Co.), and the electrode patterns were created in an electron-beam lithography process. After developing, the samples were loaded in an electron beam evaporator, and 20 nm of Ti was deposited, followed by 130 nm of Au. After the lift-off process, the samples were usually annealed to remove the fabrication residues. The electrical transport properties were measured in a commercial probe station with parametric test equipment (Agilent E5270A). The Au electrode pads were in direct contact with the Au probe tips (diameter = 5 μm). A light emitting diode (Mightex System LEDs, 365 nm) was used as the light source.

Table S1. Comparison of photocurrent (I_p), excitation wavelength (λ_{exc}), responsivity, and detectivity of Cd_2As_2 NW photodetector with previous reported work on the negative photoconductance of NWs.

Materials	I_{off}	I_p[a]	λ_{exc}	R (A W^{-1})[b]	EQE[b]	D* (Jones)[d]	Ref.[e]
InAs	3.7 μA at 1 V	1 μA	532 nm (80 mW cm^{-2})			--	S4 [37]
InAs	600 nA at 0.2 V	600 nA	500 nm (64 mW cm^{-2})	3.4×10^4	7.5×10^4	--	S5 [38]
InAs	10 μA at 1 V (at 460 K)	5 μA	450 nm (30 mW cm^{-2})	--	--	--	S6 [39]
InAs	3 μA at V= 0.3 V (with V_G= 20 V)	15 μA	633 nm (0.971-971W cm^{-2})	--	--		S7 [40]
InAs	0.45 μA at 10 mV	0.45 μA	Halogen lamp (30 mW cm^{-2})	--	--	--	S8 [41]
Cd_3As_2	25 μA at 0.3 V	2 μA	365 nm (60 mW cm^{-2})	3×10^4	2×10^5	3×10^{11}	Present work

[a] Photocurrent (= I_{on}-I_{off}), where I_{on} and I_{off} is the current under on and off condition of light illumination.

[b] Spectral responsivity (R), defined as the photocurrent generated when light of unit intensity shines on the effective area of NW, can be expressed as $R = I_p/PA$, where P is the incident light intensity and A is the effective area of NW.

[c] Photoconductive gain or external quantum efficiency (EQE), defined as $R \times (h\nu/e)$, where $h\nu$ is photon energy and e is electron charge,

[d] Specific detectivity (D*) in a unit of Jones (i.e., cm · $Hz^{1/2}$ W^{-1}). When the noise from dark current is small, it can be defined as $D^* = R\ (A/2eI_{off})^{1/2}$.

[e] The number in the bracket represents the reference number in the text.

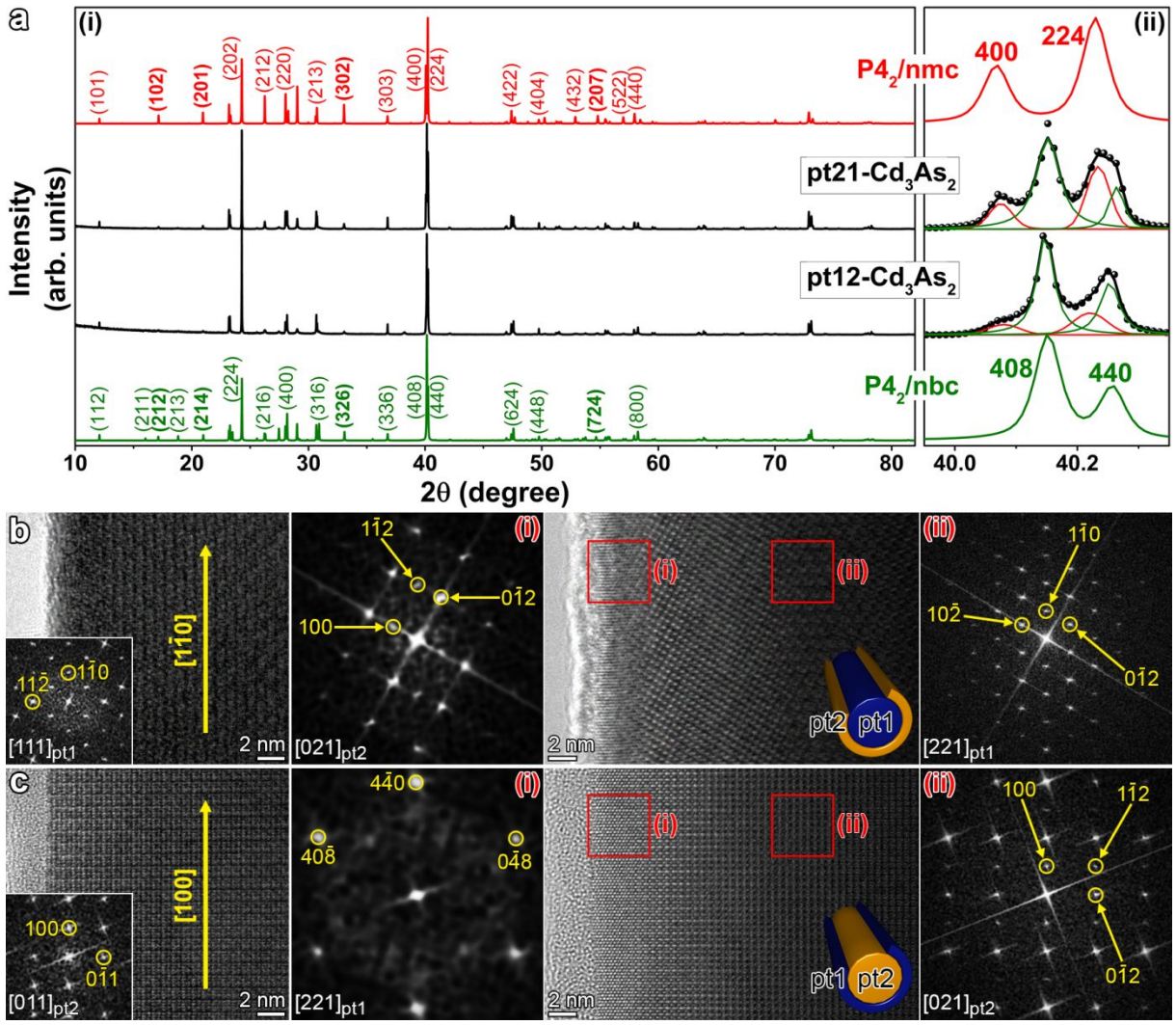

Figure S1. (a) XRD pattern of Cd_3As_2 NW grown at 380 and 420 °C, which are referred to as *pt12* and *pt21*, respectively. (i) The peaks were referenced to the $P4_2/nbc$ (a = 12.662 Å and c = 25.452 Å), and $P4_2/nmc$ (a = 8.994 Å and c = 12.622 Å) point group of primitive tetragonal phase. (ii) Magnified peaks in 2θ = 39.8-40.5 degrees. The data points (circles) are fitted by a Voigt function, and the sum of the resolved bands is represented by the black line. HRTEM and corresponding FFT images of (b) *pt12*-Cd_3As_2 and (c) *pt21*-Cd_3As_2 NWs. The inset is a schematic diagram for the core-shell NW.

(a) The magnified XRD peaks of *pt12*-Cd_3As_2 and *pt21*-Cd_3As_2 NWs, in the range of 2θ = 39.8–40.5° are resolved into four peaks: (408)/(440) peaks of *pt1* phase (green) and (400)/(224) peaks

of *pt2* phase (red), indicating that they consisted of the *pt1* and *pt*2 phases with the ratio of 4:1 and 6:4. The XRD data clearly showed that as the growth temperature increases, the phase conversion from the *pt1* to the *pt2* occurs.

(b) HRTEM and corresponding FFT images of *pt12*-Cd_3As_2 NW grown at 380 °C. The XRD pattern also shows the coexistence of *pt1* and *pt2* phases with a ratio of 4:1. At the zone axis of $[111]_{pt1}$, the growth direction was identified as $[1\bar{1}0]_{pt1}$. As the NW was rotated, different FFT images were generated for the outer and inner parts marked by squares. The inner part (i) shows the diffraction pattern at the zone axis of $[221]_{pt1}$. The outer part (ii) shows the diffraction pattern corresponding to those of *pt2* phase at the zone axis of $[021]_{pt2}$. Hence, we conclude that this Cd_3As_2 NW consisted of *pt1* and *pt2* phases in the core and shell parts, respectively. A schematic diagram of the core-shell NW structures is shown in the inset.

(c) HRTEM and corresponding FFT images of *pt21*-Cd_3As_2 NW grown at 420 °C. The XRD pattern also shows the coexistence of *pt1* and *pt2* phases with a ratio of 6:4. At the zone axis of $[011]_{pt2}$, the growth direction is identified as $[100]_{pt2}$. The $[011]_{pt2}$ axis is equivalent to $[111]_{pt1}$. As the NW was rotated toward the zone axis of $[021]_{pt2}$, the inner (i) and outer (ii) parts showed different FFT images. For the inner part, the diffraction pattern was assigned to those of *pt2* phase at the zone axis of $[021]_{pt2}$. For the outer part, the pattern was assigned to those of *pt1* phase at the zone axis of $[221]_{pt1}$. The growth direction is $[1\bar{1}0]_{pt1}$ is matched with the growth direction ($[100]_{pt2}$) of the inner part. The results indicate that the Cd_3As_2 NW consisted of two *pt1* and *pt2* phases at the core or shell parts. The inset is a schematic diagram for the core-shell NW. The matched crystallographic axes of the core/shell parts mean that the NW had a single-crystalline nature.

We observed that 80% of NWs grown at 380 and 420 °C consisted of the *pt1* and *pt2* phase, respectively, and the rest of them has both *pt1*and *pt2* phases within the single NW. It was found that the two phases exist at the core or shell part and shares the same crystallographic axes to form a single-crystalline nature. The less stable phase at a given temperature can be grown at the surface region, probably due to the kinetically controlled growth.

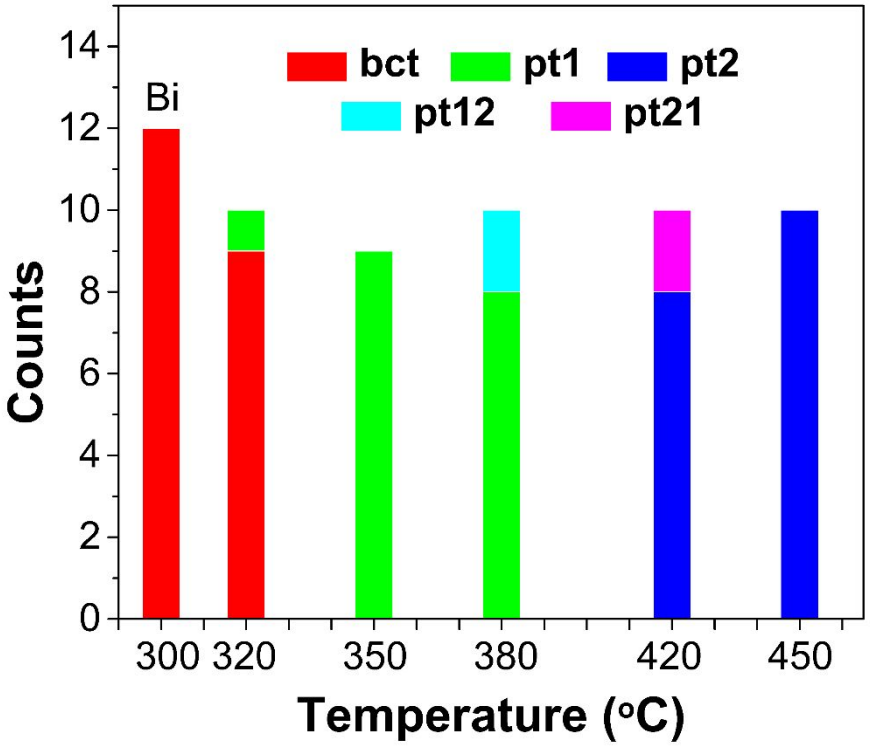

Figure 2. Fraction of phase and structures as a function of growth temperature.

For Au catalyst, high-density Cd_3As_2 NWs were grown over the temperature range of 320-450 °C. At temperatures below 320 °C or above 450 °C, the yield of NWs was much reduced. At 320 °C, 90% of NWs is in the *bct* phase, while 10% in the *pt1* phase. As the growth temperature increases to 350 °C, only *pt1* phase was observed. At 380 °C, 80% of NWs is in the *pt1* phase and 20% exists with *pt1-pt2* core-shell structure *(pt12*). At 420 °C, 80% NWs consisted of the *pt2* phase while 20% NWs consisted of *pt2-pt1* core-shell structure (*pt21*). As the growth temperature increases to 450 °C, all of NWs were grown with the *pt2* phase. In the case of Bi catalyst, high-density NWs were grown at 280-300 °C, with only *bct p*hase. When the temperature is lower or higher than 280-300 °C, the yield of NWs becomes much lower.

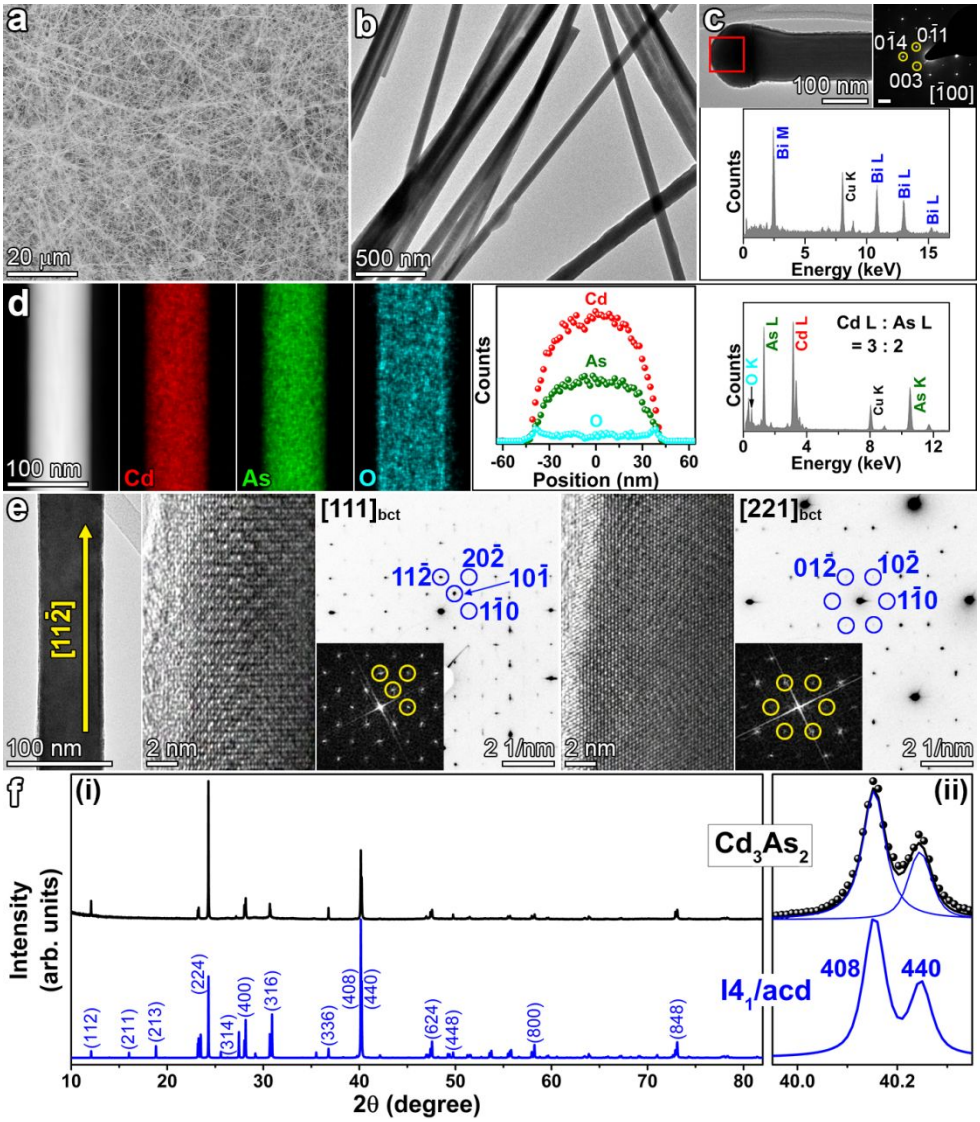

Figure S3. (a) SEM image of *bct* phase Cd_3As_2 NWs grown on a Bi-deposited Si substrate, and (b) HRTEM image, showing a general morphology of Cd_3As_2 NW. (c) HRTEM image for a catalytic nanoparticle at the tip, and its SAED pattern (zone axis = $[\bar{1}00]$) corresponding to the rhombohedral-phase Bi. EDX spectrum shows the Bi tip. (d) HAADF STEM image and EDX mapping/spectrum of Cd_3As_2 NW. (e) Lattice-resolved TEM and corresponding FFT images (insets) as well as SAED pattern (zone axis = $[111]_{bct}$ and $[221]_{bct}$). (f) XRD pattern of Cd_3As_2 NW grown on a Bi-deposited Si substrate. (i) The peaks were referenced to the $I4_1/acd$ (a = 12.665 Å and c = 25.443 Å) point group of body-centered tetragonal phase. (ii) Magnified peaks in 2θ = 39.8-40.5 degrees. The data points (circles) are fitted by a Voigt function, and the sum of the resolved bands is represented by the black line.

(a), (b) The *bct*- phase Cd_3As_2 NWs were grown on a Bi-deposited Si substrate, with high-density. The diameter has a wider range of 60–150 nm, with an average value of 80 nm.

(c) HRTEM image for a catalytic nanoparticle at the tip, and its SAED pattern (zone axis = $[\bar{1}00]$) corresponding to the rhombohedral-phase Bi (JCPDS Card No. 44-1246, $R\bar{3}m$, a = 4.547 Å and c = 11.861 Å). EDX spectrum shows the Bi tip. It suggests that the NWs were grown on the Bi (melting point = 272 °C) droplet via the VLS mechanism. The concentration of Cd in the Bi nanoparticle is negligibly small, which indicates the lower growth rate compared to that of Au catalyst.

(d) HAADF STEM image and EDX mapping/spectrum of Cd_3As_2 NW. The Cd and As elements distribute homogeneously over whole nanowire and the atomic ratio of Cd:As is 3:2 using the peaks of Cd L shell and As L shell. The EDX line profile of Cd and As elements across the nanowire, showing the homogeneous distribution of Cd and As and the O at the shell region. They are usually sheathed with oxide layer with a thickness of 2-3 nm

(e) Lattice-resolved TEM and corresponding FFT images (insets) as well as SAED pattern of (b) Cd_3As_2 (zone axis = $[111]_{bct}$ and $[221]_{bct}$). As the TEM grid holder was tilted to rotate NW, the zone axis was changed from the $[111]_{bct}$ to the $[221]_{bct}$. The growth direction is $[11\bar{2}]_{bct}$. The same SEAD pattern and FFT image was generated for the whole NW, confirming the single-crystalline nature. At the zone axis of $[221]_{bct}$, the spots nearest the zero diffraction one (as marked by circles), *i.e.*, $[01\bar{2}]$, $[10\bar{2}]$, $[1\bar{1}0]$, etc., are very weak, consistently with those synthesized using the Au catalyst.

(f) Full-range XRD patterns shows that the peaks of Cd_3As_2 NWs are matched to the lattice constants of $I4_1/acd$ space group as a = 12.665 Å and c = 25.443 Å. The (408) and (440) peaks in the range of 2θ = 39.8–40.5° were well-fitted to the reference peaks (*bct* phase) using a Voigt function. The intensity of (224) peak is higher than that of Au catalyst samples, probably due to the [112] growth direction. Wang *et al.* reported that the CVD growth of *bct* phase Cd_3As_2 nanowires at the higher and lower growth temperatures (700 °C vs. 650 °C) results in the [110] and [112] growth direction, respectively.[S9] Our result is consistent with their results; [110] vs. [112] at 320 °C vs. 300 °C.

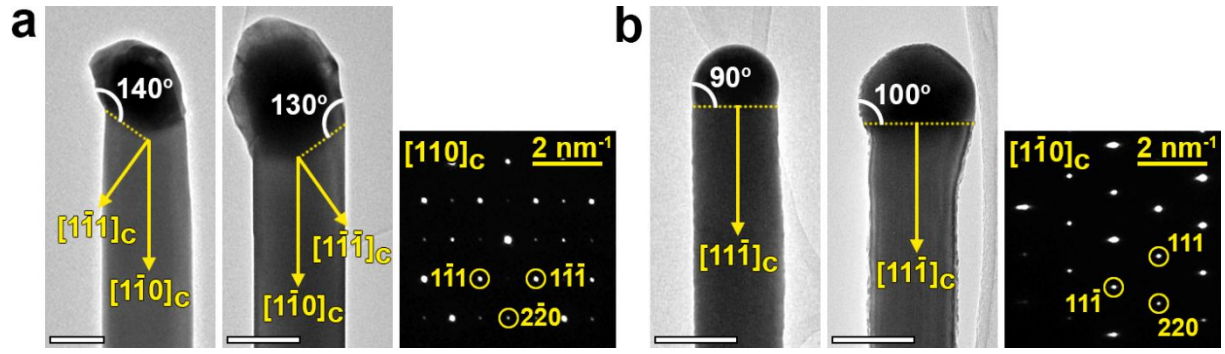

Figure S4. HRTEM images and selected-area electron diffraction (SAED) pattern for the Cd_3As_2 NWs (zone axis = $\langle 110 \rangle_C$) with (a) Au and (b) Bi nanoparticles at the tip. The growth temperature is 350 and 300 °C, respectively. Scale bars represent 100 nm. All lattices were indexed using the cubic unit cell.

At the zone axis of $\langle 110 \rangle_C$, the Au catalyst-NW interface consisted of Cd_3As_2 $(111)_C$ plane and it's direction has a tilt angle (35.3°) relative to the $[110]_C$ growth direction. In contrast, the spherical shaped Bi catalyst has flat (111) plane whose direction is aligned to the $[111]_C$ growth direction. The contact angle between the Au catalyst and the Cd_3As_2 (111) plane is 130 or 140°, while that of the flat interface of Bi-Cd_3As_2 is 90 or 100°.

The cell parameter a of the tetragonal unit cell of $I4_1/acd$ (a = 12.665 Å and c = 25.443 Å) and $P4_2/nbc$ (a = 12.662 Å and c = 25.452 Å) is close to twice the edge of the cubic unit cell, $c \approx 2a$ = 12.7 Å. The parameter a and c of $P4_2/nmc$ unit cell (a = 8.994 Å and c = 12.622 Å) has a correlation of $c = \sqrt{2}\ a$, so the unit cell can be assumed to be that of cubic cell with $c \approx 12.7$ Å. Therefore, we can analyze the crystal structure of Cd_3As_2 NWs using their pseudo cubic unit cells with the lattice constant of 12.7 Å. For the Au catalyst, the $[110]_{bct \text{ or } pt1}$ (= $[100]_{pt2}$) growth direction of the tetragonal unit cell is the same as $[110]_C$ of the cubic unit cell. In the case of Bi catalysts, the $[112]_{bct}$ growth direction of the tetragonal unit cell corresponds to $[111]_C$ of the cubic unit cell. Our group reported that the growth direction of tetragonal phase Zn_3P_2 and Zn_3As_2 NWs is $[110]_C$ for the Au catalysts, while $[111]_C$ or $[112]_C$ for the In catalyst.[S10] The growth mechanism was proposed to explain the different growth direction. The lattice parameter of the primitive tetragonal phase Zn_3P_2 (JCPDS Card No. 74-1156; $P4_2/nmc$, a = 8.097 Å and c = 11.450 Å) and Zn_3As_2 (JCPDS Card No. 30-1472; $P4_2/nbc$, a = 11.78 Å and c = 23.635 Å) was approximated as that of a cubic cell based on the correlations; $c = \sqrt{2}\ a$ for Zn_3P_2 and $c = 2a$ for Zn_3As_2. Since there is a

similarity between Zn_3P_2/Zn_3As_2 and Cd_3As_2 NWs, we assume the same growth model holding for the present Cd_3As_2 NWs.

In the cubic phase, the surface energies of the crystallographic planes could be arranged in the following order: $\{111\}_C < \{100\}_C < \{110\}_C$. The precipitation on the $(111)_C$ surface during growth along the $[110]_C$ direction would produce the largest decrease in the Gibbs free energy. The contact angle between the Au nanoparticle and the Cd_3As_2 (111) top facet is usually larger than 130 or 140°. The higher concentration of Cd in the Au droplet (Cd:Au = 7:3, as shown in Figure 2c) together with its larger contact angle (having a higher surface energy) would increase the growth rate and favor the cubic phase growing preferentially along the $[110]_C$ direction.

In the case of Bi catalyst, the concentration of Cd in the Bi nanoparticle is zero (see Figure S3c), which indicates the lower growth rate compared to that of Au catalyst. The lower contact angle of Bi catalyst than that of Au catalyst is another indication of the lower growth rate. The lower growth rate is also related with the growth temperature. Since the Cd atoms dissolved negligibly in the Bi droplet, the $(111)_C$ flat interface would be formed along the [111] growth direction. The Cd and As precursors adsorbed and accumulated on the surface, so the edge of the NW-Bi interface can be highly supersaturated. The nucleation under supersaturation conditions enables the growth along the [111] direction. Nevertheless, as these considerations are mainly speculative, further studies are probably required to elucidate the growth mechanism of Cd_3As_2 NWs.

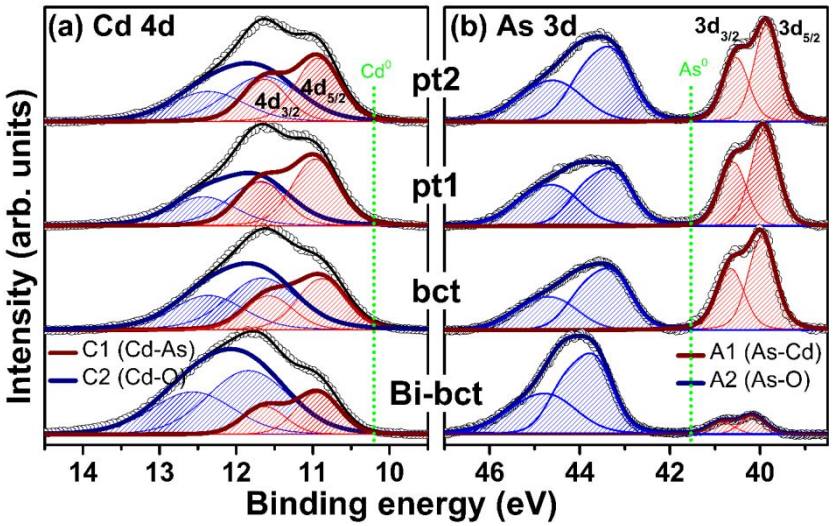

Figure S5. Fine-scanned XPS data of (a) Cd 4*d* and (b) As 3*d* peaks for Bi-*bct*-Cd_3As_2 (synthesized using Bi catalyst), *bct*-Cd_3As_2, *pt1*-Cd_3As_2, and *pt2*-Cd_3As_2. The position of the neutral Cd $3d_{5/2}$ (Cd^0) and As $3d_{5/2}$ peak (As^0) is marked by a vertical dotted line to delineate the blueshift or redshift. The raw XPS data (open circles) are fitted by a Voigt function. The sum of the resolved $d_{5/2}$ and $d_{3/2}$ bands is represented by the wine or navy line, and the sum of all bands is represented by black line. The photon energy is 630 eV.

All samples have the Cd 4*d* peak at 11.8 eV. The position of Cd $4d_{5/2}$ and $4d_{3/2}$ peaks (separated by 0.7 or 0.9 eV) for metal (Cd^0) are known to be 10.2 and 10.9 (or 11.1) eV.[S11] The peak was resolved into two bands with the $4d_{5/2}$ peak at 10.9 eV and 11.6 eV, which are ascribed to the Cd-As (C1 band) and Cd-O (C2 band) bonding structures, respectively. The ratio of C2/C1 bands at 380 eV is close to 1 for the Cd_3As_2 NWs grown using the Au catalyst, while it is 2 for the Cd_3As_2 grown using the Bi catalyst.

The As $3d_{5/2}$ and $3d_{3/2}$ peaks (separated by 0.7 eV) of As-Cd (A1 band) appears at 40.0 and 40.7 eV, which are red shifted with respect to that of neutral As at 41.6 eV ($3d_{5/2}$), corresponding to the anion binding to the Cd cations. The As-O (A2) bands appear at 44 eV. It suggests that the surface defects can form the oxide layers. The *bct*-Cd_3As_2 (Bi), which was synthesized using the Bi catalysts, shows the significant As-O peak than those of NW synthesized using Au catalysts, due to the thicker surface oxide layers. The ratio of As-O/As-Cd bands is about 1 for the Cd_3As_2 NWs grown using the Au catalyst, while it is about 8 for the Cd_3As_2 grown using the Bi catalyst. For this 630 eV photon energy, the probe depth of XPS is below 1 nm.[S12] Therefore the oxide peaks originate solely from the surface region of the Cd_3As_2 NWs.

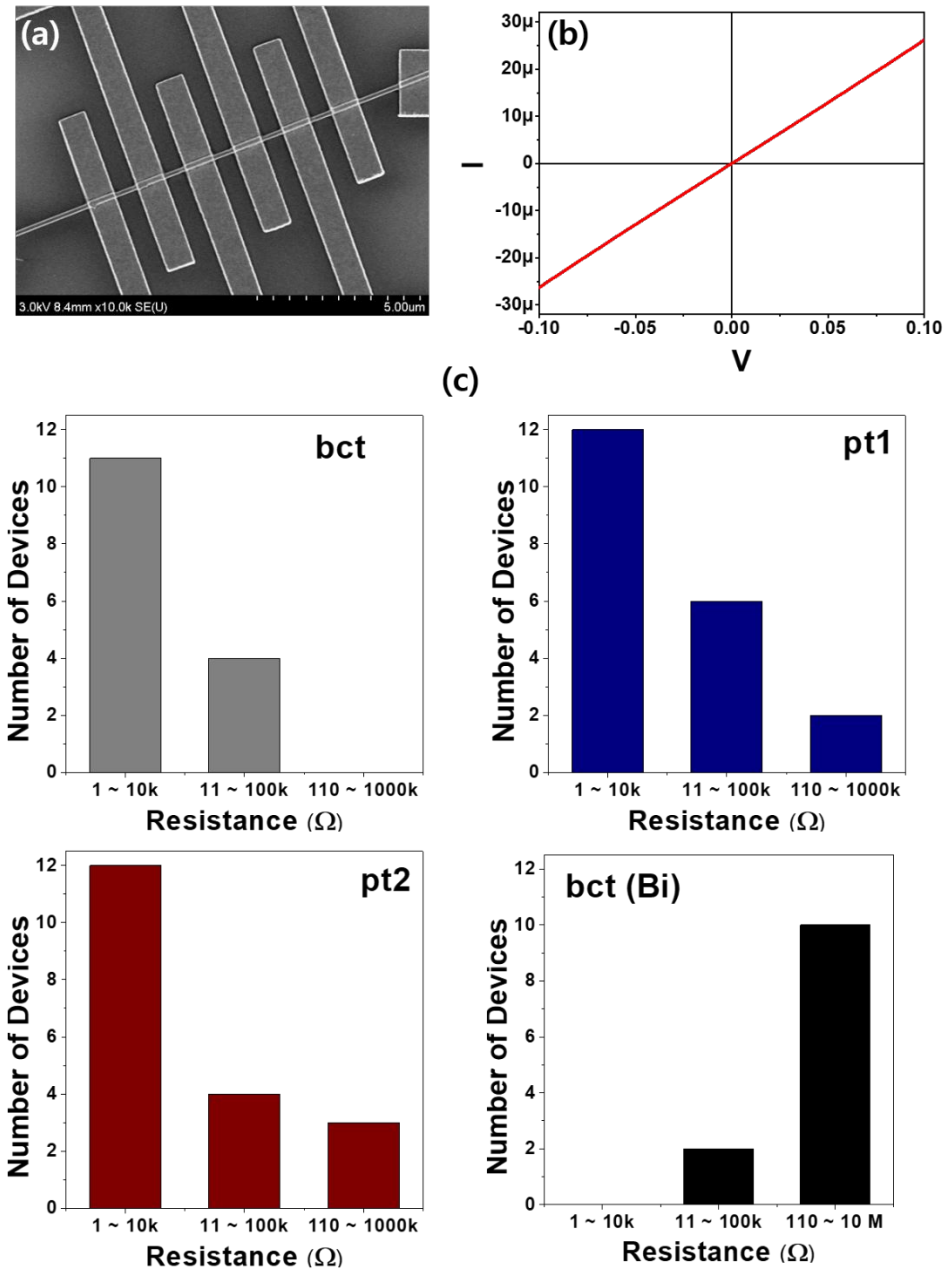

Figure S6. (a) SEM images of the Cd_3As_2 NW electrode. (b) Typical Ohmic contact current-voltage (I-V) characteristics of typical Cd_3As_2 NW under dark condition. (c) Histogram for the resistance (Ω) of *bct*-Cd_3As_2, *pt1*-Cd_3As_2, *pt2*-Cd_3As_2, and Bi-*bct* phase Cd_3As_2 (synthesized using the Bi catalyst) NW electrodes. The distribution of resistance shows that 70% has 1-10 kΩ for Cd_3As_2 NW (synthesized using the Au catalyst) corresponding to the conductivity of 10^4 S/cm. However, the majority of *bct*-Cd_3As_2 (synthesized using the Bi catalysts) NW electrodes have the resistance of 10 MΩ, corresponding to the conductivity of 10^2 S/cm.

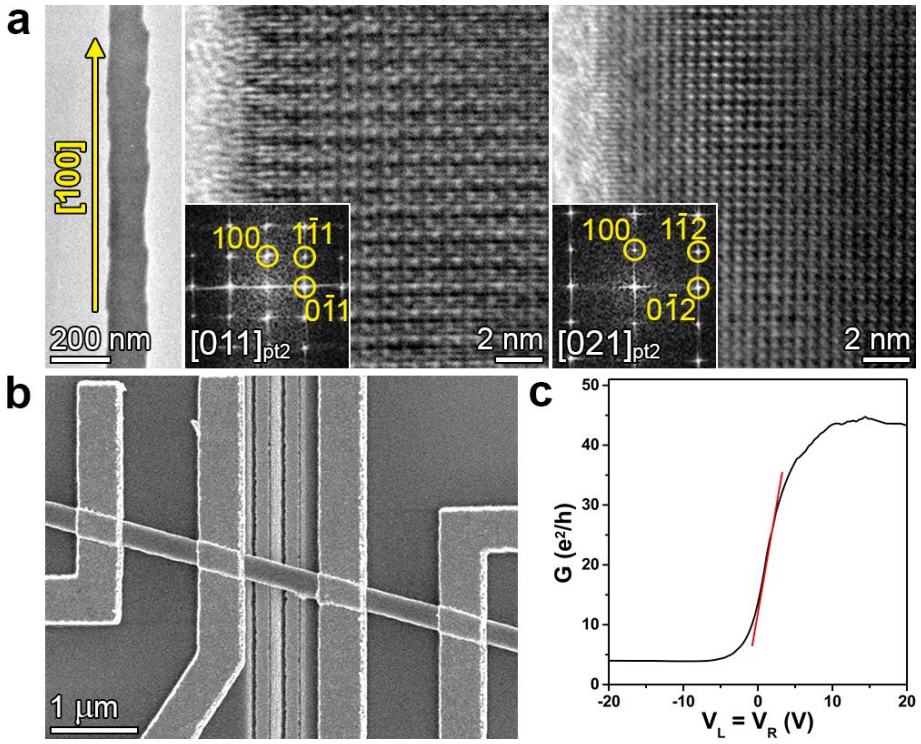

Figure S7. (a) HRTEM and corresponding FFT images (zone axis = $[011]_{pt2}$ and $[021]_{pt2}$) of Cd_3As_2 nanoribbon, (b) SEM image of four-terminal FET device fabricated using a *pt2*-Cd_3As_2 nanoribbon. The two bottom gates are controlled by V_L and V_R. (c) Conductance measured for *pt2*-Cd_3As_2 nanoribbon as a function of diagonal gate voltage ($V_R = V_L$).

The nanoribbons are frequently grown with the NWs at 450 °C. The HRTEM and corresponding FFT images of *pt2*-Cd_3As_2 nanoribbon (width = 150 nm) show the single crystalline nature with the [100] long axis, which is the same as the growth direction of *pt2*-Cd_3As_2 NWs. Four terminal FFT device was fabricated using the *pt2*-Cd_3As_2 nanoribbon. The width of nanoribbon is 270 nm, which is much larger than the thickness (80 nm, confirmed by atomic force microscopy). So this nanoribbon is an appropriate model for a 2D sheet. Using the parallel-plate capacitor model, we extracted the mobility of 5.4×10^4 cm^2/Vs, which is similar to those of nanowires. The calculation of mobility is shown below.

W (nm)	L (nm)	A (nm^2)	C (F)	slope	dG/dV_G	μ ($cm^2\ V^{-1}s^{-1}$)
270	900	2.43×10^5	3.07×10^{-17}	5.27	2.04×10^{-4}	5.4×10^4

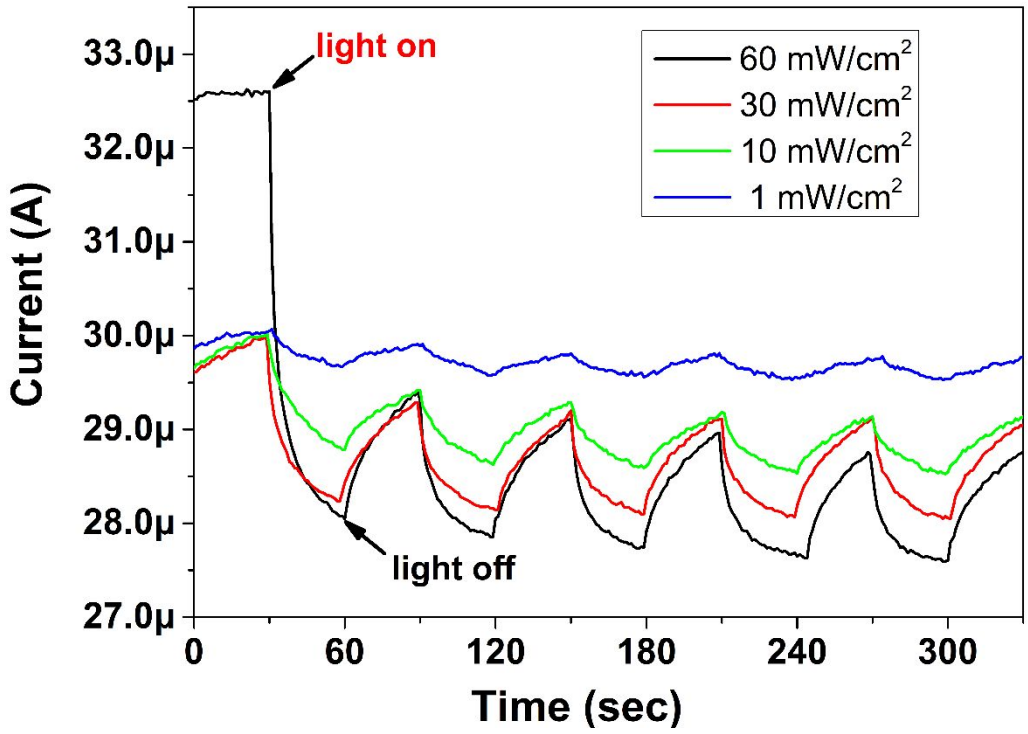

Figure S8. I-t curves of Cd_3As_2 NW photodetectors (showing NPC) at a bias voltage (V_{DS}) of 0.3 V in real time under a series of different intensity of 365 nm irradiation. Each on-off curve was measured with a sequence of 60 → 30 → 10 → 1 mW/cm^2. As the light intensity decreases, the magnitude of negative photocurrent decreases without any change from negative to positive value.

References

(S1) Martel, R.; Schmidt, T.; Shea, H. R.; Hertel, T.; Avouris, Ph. Single- and Multi-Wall Carbon Nanotube Field Effect Transistors. *Appl. Phys. Lett*. **1998**, *73*, 2447.

(S2) Vashaee, D.; Shakouri, A.; Goldberger, J.; Kuykendall, T.; Pauzauskie, P.; Yang, P. Electrostatics of Nanowire Transistors with Triangular Cross Sections. *J. Appl. Phys*. **2006**, *99*, 054310.

(S3) Gül, O.; van Woerkom, D. J.; van Weperen, I.; Car, D.; Plissard, S. R.; Bakkers, E. P. A. M.; Kouwenhoven, L. P. Towards High Mobility InSb Nanowire Devices. *Nanotechnology* **2015**, *26*, 215202.

(S4) Guo, N.; Hu, W.; Liao, L.; Yip, S. P.; Ho, J. C.; Miao, J.; Zhang, Z.; Zou, J.; Jiang, T.; Wu, S. *et al.* Anomalous and Highly Efficient InAs Nanowire Phototransistors Based on Majority Carrier Transport at Room Temperature. *Adv. Mater.* **2014**, *26*, 8203-8209.

(S5) Yang, Y.; Peng, X.; Kim, H. -S.; Kim, T.; Jeon, S.; Kang, H. K.; Choi, W.; Song, J.; Doh, Y. -J.; Yu, D. Hot Carrier Trapping Induced Negative Photoconductance in InAs Nanowires toward Novel Nonvolatile Memory. *Nano Lett.* **2015**, *15*, 5875-5882.

(S6) Fang, H.; Hu, W.; Wang, P.; Guo, N.; Luo, W.; Zheng, D.; Gong, F.; Luo, M.; Tian, H.; Zhang, X. *et al.* Visible Light-Assisted High-Performance Mid-Infrared Photodetectors Based on Single InAs Nanowire. *Nano Lett.* **2016**, *16*, 6416-6424.

(S7) Han, Y.; Fu, M.; Tang, Z.; Zheng, X.; Ji, X.; Wang, X.; Lin, W.; Yang, T.; Chen, Q. Switching from Negative to Positive Photoconductivity toward Intrinsic Photoelectric Response in InAs Nanowire. *ACS Appl. Mater. Interfaces* **2017**, *9*, 2867-2874.

(S8) Alexander-Webber, J. A.; Groschner, C. K.; Sagade, A. A.; Tainter, G.; Gonzalez-Zalba, M. F.; Pietro, R. D.; Wong-Leung, J.; Tan, H. H.; Jagadish, C.; Hofmann, S. et al. Engineering the Photoresponse of InAs Nanowires. *ACS Appl. Mater. Interfaces* **2017**, *9*, 43993-44000.

(S9) Wang, L. -X.; Wang, S.; Li, J. -G.; Li, C. -Z.; Yu, D.; Liao, Z. -M. Universal Conductance Fluctuations in Dirac Semimetal Cd_3As_2 Nanowires. *Phys. Rev. B* **2016**, *94*, 161402.

(S10) Im, H. S.; Park, K.; Jang, D. M.; Jung, C. S.; Park, J.; Yoo, S. J.; Kim, J. G. Zn_3P_2-Zn_3As_2

Solid Solution Nanowires. *Nano Lett.* **2015**, *15*, 990-997.

(S11) Poole, R. T.; Leckey, R. C. G.; Jenkin, J. G.; Liesegang, J. Photoelectron Emission and d Bands of Zinc and Cadmium. *Phys. Rev. B* **1973**, *8*, 1401-1406.

(S12) Powell, C. J.; Jablonski, A. Evaluation of Calculated and Measured Electron Inelastic Mean Free Paths Near Solid Surfaces. *J. Phys. Chem. Ref. Data* **1999**, *28*, 19-62.